Geoderma 462 (2025) 117542

Contents lists available at ScienceDirect

Geoderma

journal homepage: www.elsevier.com/locate/geoderma

# Long-term no-tillage farming mitigates waterlogging during extreme rainfall events in black soil (Mollisols) region of Northeast China

Shijie Qin [a,b], Zhuo Liu [a], Meng Tian [c], Lin Liu [a], Wei Hu [d], Richard Whalley [e], Tusheng Ren [a], Weida Gao [a,*]

[a] College of Land Sciences and Technology, China Agricultural University, Beijing 100193, China
[b] Hunan Cultivated Land and Agricultural Eco-Environment Institute, Changsha 410125, China
[c] Institute of Geographical Sciences, Henan Academy of Sciences, Zhengzhou 450015, China
[d] The New Zealand Institute for Plant and Food Research Limited, Mt Albert Road, Sandringham, Auckland 1025, New Zealand
[e] Rothamsted Research, Harpenden, St Albans AL5 2JQ, UK

ARTICLE INFO

Handling Editor: Yvan Capowiez

*Keywords:*
Pores stratification
Biopores
Waterlogging
Preferential flow

ABSTRACT

The increasing frequency of extreme rainfall events intensifies waterlogging-induced aeration stress on crops, highlighting the urgency for adaptive agricultural practices. This study evaluates the potential of long-term no-tillage (NT) farming to mitigate waterlogging risks on a silty clay loam in Northeast China by comparing with traditional moldboard plough (MP) farming using an 11-year field experiment. Rainfall simulation (40 mm $h^{-1}$) and dye-tracing were employed to study the dynamics water infiltration, and X-ray computed tomography (CT) was applied to examine soil pore characteristics (0–60 cm depth) and their responses (0–5 cm layer) to raindrop splashing. Results demonstrated that NT significantly enhanced water infiltration capacity, with a 161 % higher maximum infiltration depth (*MID*), an 65 % increase in total stained area (*TSA*), and 95 % less surface ponding compared to MP. Although MP exhibited higher total porosity ($\varepsilon_{total}$), macroporosity (>0.04 mm pores, $\varepsilon_{X\text{-}ray}$), and increased pore connectivity in the 0–20 cm layer, it had fewer biopores and greater vertical stratification of macroporosity compared to NT across the 0–60 cm profile. During rainfall events, the MP plot experienced a 28 % reduction in porosity of pores sized 0.2–1.0 mm and a 19 % increase in porosity of pores <0.2 mm in the surface layer, likely due to raindrop splashing, while NT maintained pore integrity through straw mulching. We conclude that long-term NT is effective in enhance soil resilience to waterlogging by developing continuous vertical pore networks and maintaining surface mulch, thereby improving climate adaptability in the black soil region of Northeast China.

## 1. Introduction

Global climate change has intensified extreme rainfall events, characterized by heavy rainfall or prolonged droughts (Fischer and Knutti, 2015; Piao et al., 2010). Heavy rainfall can trigger overland runoff, soil erosion, and crop hypoxia stress, thereby threatening global food security (Hess et al., 2018). Soil water infiltration capability is a primary defense against heavy rainfall, as it directly determines the partitioning of rainfall at the soil surface. A high infiltration capacity allows more water to enter the soil profile, while a low capacity causes water to accumulate on the surface or in the root zone during or after downpour events. This capability is strongly influenced by farming practices (Cynthia et al., 2002; Hess et al., 2018). Conservation management like no-tillage (NT) farming offers agronomic and environmental benefits and are widely adopted (Fernández-Ugalde et al., 2009; Govindasamy et al., 2020). However, there lacks consensus on the impact of NT on water infiltration capacity (e.g., Blanco-Canqui et al., 2017; Fan et al., 2013; Moraes et al., 2016). This disagreement may stem from how NT management shapes the soil pore network and how this interacts with rainfall conditions.

A key mechanism through which tillage practices influence infiltration is by altering soil pore architecture. Previous studies have primarily assessed water infiltration into soils using the methods such as constant head infiltration on intact cores in lab, single or double-ring infiltration

* Corresponding author.
*E-mail addresses:* sjqin@cau.edu.cn (S. Qin), liuzhuo_99@cau.edu.cn (Z. Liu), m18814116485@163.com (M. Tian), linliu@cau.edu.cn (L. Liu), Wei.Hu@plantandfood.co.nz (W. Hu), richard.whalley@rothamsted.ac.uk (R. Whalley), tsren@cau.edu.cn (T. Ren), weida_gao@cau.edu.cn (W. Gao).

https://doi.org/10.1016/j.geoderma.2025.117542
Received 22 July 2025; Received in revised form 27 September 2025; Accepted 5 October 2025
Available online 10 October 2025

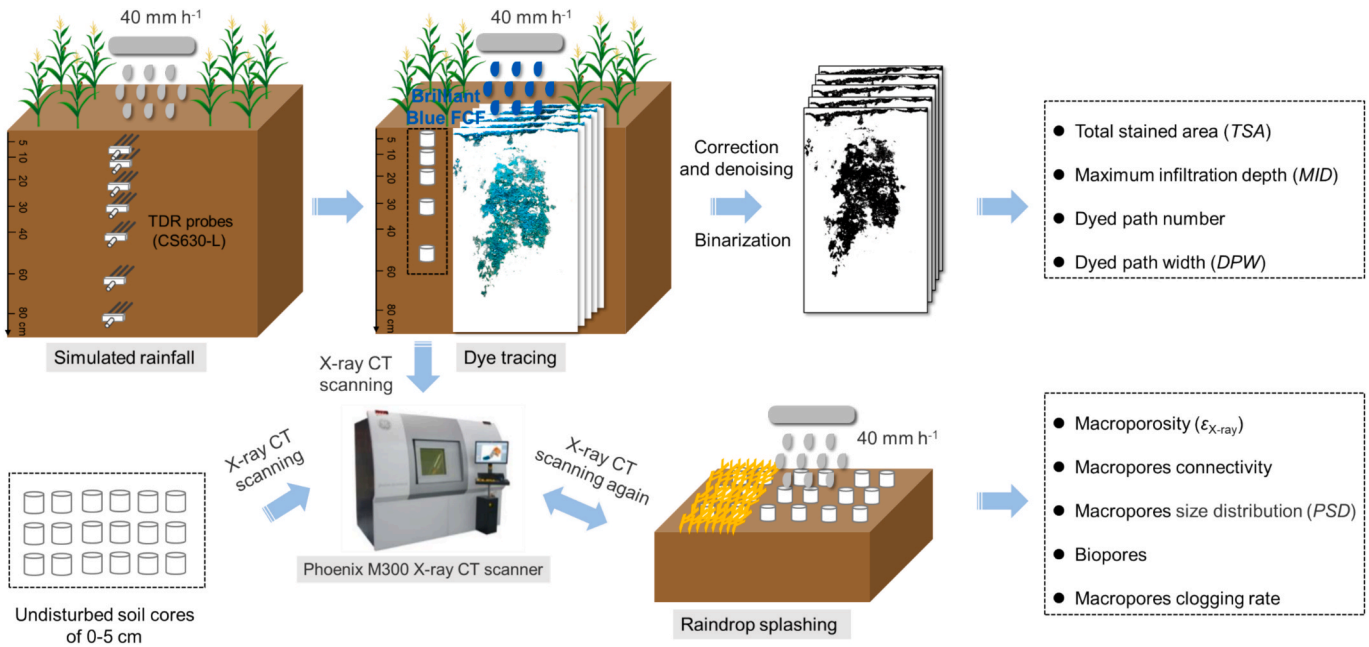


**Fig. 1.** Schematic diagram of experimental design.

in field, dye tracing, and various infiltration models (Fan et al., 2013; Haruna et al., 2024; Soracco et al., 2019). Specifically, the co-occurrence and connectivity of macropores throughout the soil profile are crucial for facilitating rapid water movement via preferential flow paths (Allaire-Leung et al., 2000). However, soil core results inadequately represent profile-scale infiltration because they sample a limited volume and miss structural connectivity (e.g., macropore connection) between soil layers, an important factor influencing soil water movement. Moldboard plow (MP) farming typically increased topsoil porosity and connectivity but can disrupt subsoil pores and created a plow pan, reducing vertical connectivity due to tillage disturbance (Wardak et al., 2024). In contrast, long-term NT management promotes the development of stable biopores (e.g., former root channels and earthworm burrows) and enhances their continuity across soil layers, creating a more connected and efficient pore network (Budhathoki et al., 2022; Wardak et al., 2024). These biopores act as hydraulically efficient preferential flow paths, transferring water more rapidly and deeply into the subsoil than irregular non-biopores due to their greater structural stability, lower tortuosity, and smoother walls (Mestelan et al., 2021; Pagenkemper et al., 2015; Zhang et al., 2019). However, NT can also lead to higher surface bulk density, particularly in fine-textured soils, which may initially hinder infiltration (Blanco-Canqui et al., 2017), highlighting the complex trade-off between pore connectivity and topsoil conditions under NT.

Although field measurements using single or double-ring infiltrometers and dye tracing can reflect the effects of pore networks within soil profile, they are often conducted under simulated ponding without rainfall, thus failing to account for the disruptive effects of raindrop impact on surface soil structure. Raindrops dynamically alter soil structure during rainfall, with splashing disaggregating soil particles and sealing surface soil pores, potentially reducing infiltration by 11–56 % (Assouline, 2004; Legout et al., 2005; Ma et al., 2022). A key advantage of NT systems is the presence of a protective straw mulch buffer layer, which can effectively mitigate raindrop splash's negative effects on soil structure under NT (Almeida et al., 2018; Gómez-Paccard et al., 2015). Consequently, infiltration measurements under non-rainfall conditions may misrepresent the actual effects of tillage management, particularly for NT whose benefits are tied to both subsurface pore connectivity and surface protection.

In this study, we hypothesized that long-term NT farming enhances infiltration during extreme rainfall by maintaining profile-wide macropore continuity and straw mulching's buffering effects. The objectives of this study were to (1) characterize water infiltration and flow patterns under NT and MP during extreme rainfall events, and (2) explore the underlying mechanisms from the perspective of soil pore system—considering both surface protection and subsurface connectivity—using high-frequency soil water content monitoring, dye tracers, and X-ray CT.

## 2. Materials and methods

### 2.1. Study site

We used a long-term farming system experiment initiated in the spring of 2011 at the Lishu Experiment Station of China Agricultural University, Jilin Province (43°16′ N, 124°26′ E), China. The region has a sub-humid monsoon climate with an average annual temperature of 5.9 °C and precipitation of 556 mm. The soil is classified as Mollisol (Mollisol, USDA) with a silty clay loam texture (17.2 % sand, 46.1 % silt, and 36.7 % clay) and an organic matter content of 21.0 g $kg^{-1}$ (Soil Survey Staff, 2022).**

This study compared two treatments: no-tillage (NT) farming and traditional moldboard plough (MP) farming, both with mono-cropped maize (*Zea mays L.*). Each treatment had three replications, with plots measuring 21.6 m by 63.0 m. Under NT, ~6000 kg $ha^{-1}$ of crop residue remained on the soil surface at ~30 cm stubble height. For the MP treatment, maize residue was removed from the field after harvesting and soil was tilled to a depth of about 20 cm using a moldboard plow the following spring. For both treatments, maize was planted in May using a paired-row no-till seeder (2BMZF-2, Jilin Province Kangda Agricultural Machinery Group Co. Ltd.). The two treatments received equal fertilizer application (800 kg $ha^{-2}$, N-$P_2O_5$-$K_2O$ (26-10-12)) and were maintained at a planting density of 63,000 seeds per hectare. No irrigation was applied during the growing season. We applied herbicides at post-sowing to control weeds in both treatments. Maize was harvested using a combine harvester (4YL-6(R230), John Deere (Jiamusi) Agricultural Machinery Co. Ltd.) in the fall.

### 2.2. Field studies on soil water infiltration

#### 2.2.1. Simulated rainfall experiments

Simulated rainfall experiments were conducted to compare the infiltration characteristics of the NT and MP systems. The rainfall-simulator consisted of a peristaltic pump (FB-I/104kA, Chongqing Jieheng Peristaltic Pump Co. Ltd.) that maintained a 4 cm water column pressure between two 50 × 50 cm acrylic glass plates, each equipped with 196 evenly spaced 26 G cannulas (Marquart et al., 2020) (Fig. S1). The rainfall-simulator was mounted on a 70 cm-high steel frame, positioned over a 50 × 50 cm plot, and enclosed with plastic film to prevent wind interference with raindrop trajectories. To minimize lateral water seepage, a stainless-steel frame (10 cm in height, 0.2 cm thickness) was inserted 5 cm into the soil beneath the setup. A 10-cm long steel ruler was placed vertically within the plot to measure surface water depth at a 10-minute interval. The rainfall intensity was set to 40 mm $h^{-1}$ based on local extreme rainfall data (Fig. S2). Each tillage treatment underwent six replicated rainfall simulations, with each event lasting one hour. Adjacent events were spaced several hours apart to ensure consistent initial volumetric water content across replicates (Table S1).

During the rainfall simulation studies, volumetric soil water content ($\theta$) was monitored using time-domain reflectometry (TDR). A pit was excavated at the infiltration site, and seven pre-calibrated TDR probes (CS630-L, Campbell Scientific, Logan, UT, USA), with 15 cm-long, 0.32 cm-diameter rods were installed at depths of 5, 10, 20, 30, 40, 60, and 80 cm in both NT and MP plots (Fig. 1). To reduce soil disturbance, the probes were installed 45 days before the rainfall simulation experiment. The sensors were connected to a TDR200 system (Campbell Scientific, Logan, UT, USA) controlled by a CR1000X data logger (Campbell Scientific, Logan, UT, USA). The $\theta$ values were recorded at a 3-minute interval to accurately capture infiltration dynamics.

#### 2.2.2. Dye tracer experiment

To visualize water flow paths under NT and MP treatments, we performed a dye-tracing experiment immediately after the simulated rainfall study in the same plots. We used Brilliant Blue FCF (4 g $L^{-1}$) as the tracer due to its low toxicity, high visibility, and excellent mobility (German-Heins and Flury, 2000; Marquart et al., 2020). The rainfall intensity and duration matched those of the previous experiment. Forty-eight hours after dye application, we excavated five soil pits (75 cm deep and 45 cm wide) to examine dye distribution though the soil profile. Soil profiles were photographed using a Sony α6400 camera (4912 × 3264 pixels, Fig. 1). We employed a linen cloth during photography to maintain consistent lighting and eliminate direct sunlight interference.

### 2.3. Characteristics of soil pores

For soil analysis following the rainfall simulation and dye-tracer experiments, we collected undisturbed soil cores from five depth intervals (0–5, 5–10, 10–20, 20–40, and 40–60 cm) using PVC tubes (5.0 cm height × 4.8 cm inner diameter, Fig. 1). Five replicate cores were randomly sampled from each layer. The cores were scanned using a Phoenix M300 X-ray CT scanner (GE Sensing and Inspection Technologies, GmbH, Wunstorf, Germany) at 160 kV beam energy and 150 μA current. After scanning, samples were oven-dried at 105 °C for 24 h, cooled to room temperature, and weighed to determine bulk density. Then, the total porosity ($\varepsilon_{total}$) was calculated with a particle density of 2.65 g $cm^{-3}$.

### 2.4. Raindrop splashing

To quantify splash erosion on the surface soil structure during simulated rainfall (Fig. 1 and S3), we conducted a raindrop splash experiment using 18 undisturbed soil cores (0–5 cm) collected near the experimental area in PVC tubes (5.0 cm height × 4.8 cm inner diameter). The samples included 12 cores were from NT plots (6 with maize straw mulch [NT], 6 bare [NT-S]) and 6 cores were from MP plots (Fig. S4). All cores were initially CT-scanned, then exposed in situ to 40 mm $h^{-1}$ rainfall (match the simulation protocol). After splash exposure, samples were carefully retrieved and re-scanned using identical CT parameters (160 kV and 150 μA).

### 2.5. Image analysis

For the dye tracer experiment, all images were geometrically corrected and denoised using Adobe Photoshop CC2018 (Adobe, San Jose, CA, USA), resulting in processed images measuring 75 × 45 cm with 3750 × 2250 pixels resolution. Following binarization in Image J (Version 1.50i, National Institute of Health, http://imagej.nih.gov/ij/), we classified soil profile into dyed and non-dyed regions.

Using MATLAB R2022a (MathWorks, Natick, MA, USA), we quantified four infiltration parameters: total stained area (*TSA*), maximum infiltration depth (*MID*), number of dyed paths, and dyed path width (*DPW*) as a function of depth (Fig. 1). *DPW* variations revealed three distinct water flow patterns: (1) <20 mm: preferential flow with minimal matrix interaction; (2) 20–200 mm: preferential flow with moderate matrix interaction or non-homogeneous matrix flow; (3) >200 mm: homogeneous matrix flow (Weiler and Flühler, 2004; Zwartendijk et al., 2017).

For the X-ray CT analysis, each soil core was scanned to acquire 1500 projections, which were reconstructed into 3D tomograms using Datos × 2.0 software (GE Sensing and Inspection Technologies, GmbH, Wunstorf, Germany) (Fig. 1). The reconstructed 8-bit greyscale images (40 μm resolution) were processed in ImageJ (Version 1.50i, National Institute of Health, http://imagej.nih.gov/ij/) with the following protocols. For general analysis, (1) A cylindrical region of interest (ROI, 920 × 789 pixels) was selected from the core center; (2) A Gaussian filter (radius = 1) was applied to reduce image noise; and (3) Pores were segmented using default thresholding (Yudina et al., 2022). For the raindrop splash analysis, an extended ROI (1100 × 1152 pixels; 0.1–4.7 cm depth range) captured surface soil structure changes, and identical filtering and segmentation methods were applied.

Macroporosity ($\varepsilon_{X\text{-}ray}$) and macropore connectivity were quantified at 40 μm resolution. Connected macropores were identified using Avizo 9.0's 'Axis Connectivity' module (Thermo Fisher Scientific, Waltham, MA, USA) (Lu et al., 2019), with connectivity expressed as the volume ratio of connected macropores to $\varepsilon_{X\text{-}ray}$. Macropores size distribution (*PSD*) was determined via the maximum inscribed spheres method, using the Thickness plugin in Image J (Hildebrand and Rüegsegger, 1997; Houston et al., 2017). Biopores were identified at 40 μm resolution using Fiji's 'Biopores' plugin (Version 1.53t, National Institute of Health, https://imagej.nih.gov/ij/), followed by removal of misclassified features using Avizo 9.0's 'Filters' module in (Lucas et al., 2019).

### 2.6. Data calculation and statistical analysis

#### 2.6.1. Data calculation

To evaluate water infiltration during the simulated rainfall period, we first determined the maximum infiltration depth (*MID*, cm) using the two-curve methods. This approach identifies the crossover points between soil water content profiles measured before and after rainfall (Guo, 2020). Based on the *MID*, soil water supply ($S_t$, mm) was calculated as the difference in $\theta$ over the soil depth $L$ (cm) before and after rainfall event:

$$S_t = \int_0^L \theta(x,t)dx - \int_0^L \theta(x,0)dx \quad (1)$$

where $t$ (min) is the time when $\theta$ ($cm^3$ $cm^{-3}$) at depth $L$ stops increasing during the rainfall event.

Wetting front velocity ($V_{wf}$, cm $min^{-1}$) (Hu et al., 2019) and average

**Table 1**
Ponding depth at different times, maximum infiltration depth (*MID*) and soil water supply ($S_t$) under no-tillage (NT) and moldboard plough (MP). Different lower-case letters indicate significant differences between tillage treatments ($P < 0.05$).

| Tillage treatments | Ponding depth (cm) | | | | | | *MID* (cm) | $S_t$ (mm) |
|---|---|---|---|---|---|---|---|---|
| | 10 min | 20 min | 30 min | 40 min | 50 min | 60 min | | |
| MP | 0.92 ± 0.32 | 1.37 ± 0.25a | 1.67 ± 0.31a | 1.85 ± 0.38a | 2.1 ± 0.53a | 2.24 ± 0.61a | 40 | 6.74 ± 2.10b |
| NT | 0 | 0.01 ± 0.03b | 0.04 ± 0.01b | 0.06 ± 0.02b | 0.06 ± 0.02b | 0.12 ± 0.19b | 60 | 13.67 ± 1.65a |

wetting rate ($S_{mean}$, $10^{-2}$ cm$^3$ cm$^{-3}$ min$^{-1}$, Tian et al., 2019) were calculated as:

$$V_{wf} = \frac{h}{t_1} \tag{2}$$

$$S_{mean} = \frac{\theta_{t_2} - \theta_{t_1}}{t_2 - t_1} \times 100 \tag{3}$$

where $h$ (cm) is the soil thickness at various depths (5, 10, 20, 30, 40, 60, and 80 cm), $t_1$ (min) is the time when the probe first detects an increase in $\theta$ ($\geq$0.005 cm$^3$ cm$^{-3}$, considering the measurement accuracy of the pre-calibrated TDR sensors), $t_2$ (min) is the time when the increase ceases, Parameters $\theta_{t_1}$ (cm$^3$ cm$^{-3}$) and $\theta_{t_2}$ (cm$^3$ cm$^{-3}$) represent the volumetric soil water content at $t_1$ and $t_2$, respectively, and 100 is a conversion coefficient.

The stratification ratio (*SR*) of $\varepsilon_{X\text{-ray}}$ and bioporosity was calculated to evaluate vertical variations of pore characteristics:

$$SR_{\varepsilon_{X-ray}\text{ or bioporosity}} = \frac{(\varepsilon_{X-ray}\text{ or bioporosity})_{0-20cm}}{(\varepsilon_{X-ray}\text{ or bioporosity})_{20-60cm}} \tag{4}$$

where $(\varepsilon_{X\text{-ray}}$ or bioporosity$)_{0\text{-}20\ cm}$ and $(\varepsilon_{X\text{-ray}}$ or bioporosity$)_{20\text{-}60\ cm}$ are detectable macroporosity and bioporosity at the 0–20 and 20–60 cm soil layers, respectively, Higher *SR* values deviating from 1 indicate greater vertical stratification of $\varepsilon_{X\text{-ray}}$ or bioporosity across the soil profile.

To quantify structural changes caused by raindrop splash, macropores clogging rate was calculated as (Ma et al., 2022):

$$\text{Macropores clogging rate} = \frac{\varepsilon_{X-ray0} - \varepsilon_{X-ray1}}{\varepsilon_{X-ray0}} \times 100\% \tag{5}$$

where $\varepsilon_{X\text{-ray0}}$ and $\varepsilon_{X\text{-ray1}}$ are the detectable macroporosity before and after raindrop splashing, respectively.

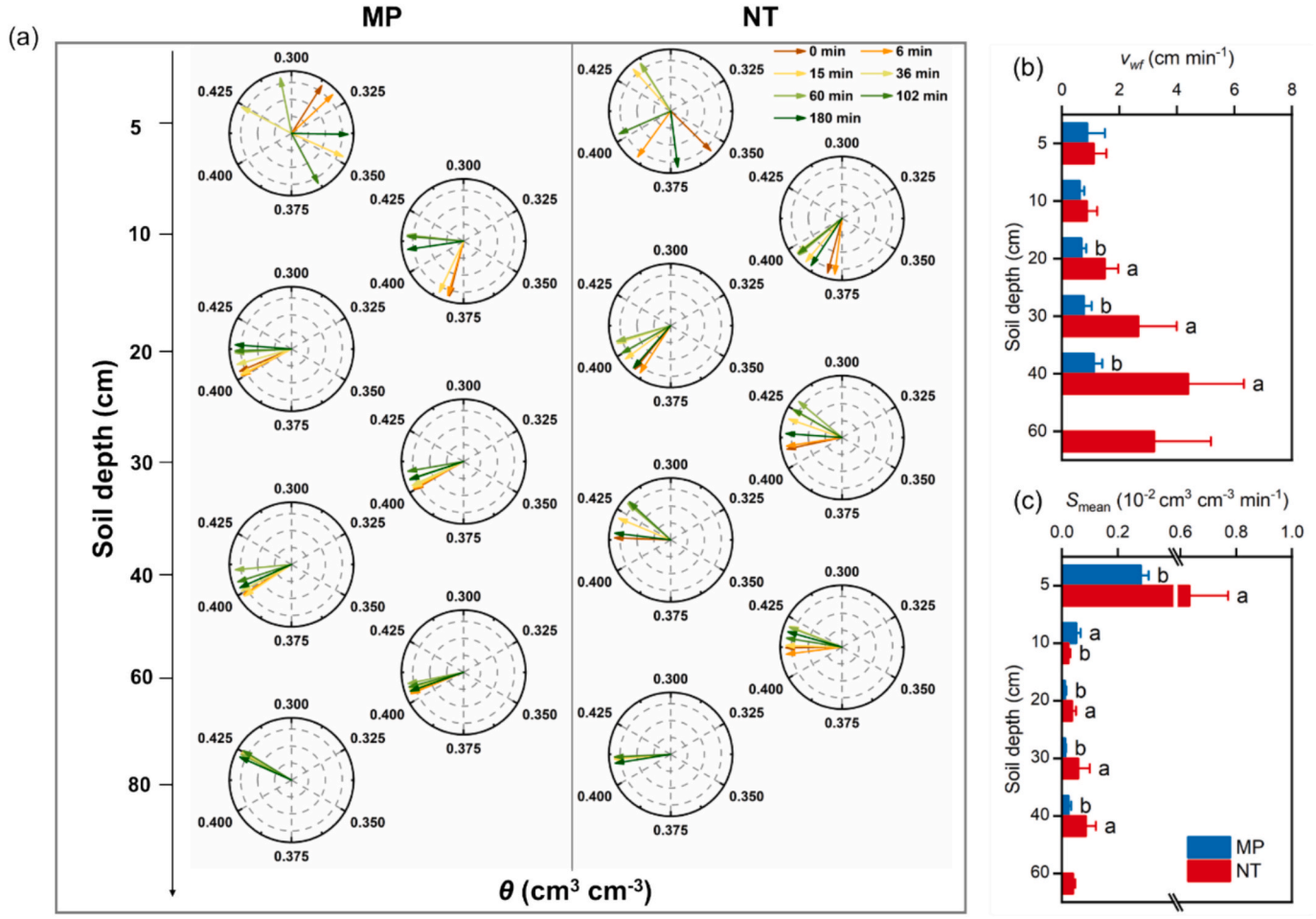


**Fig. 2.** The dynamic of soil water content ($\theta$) (a), penetration velocity of the wetting front ($V_{wf}$) (b), and average wetting rate ($S_{mean}$) (c) with depth after infiltration experiment under no-tillage (NT) and moldboard plough (MP). The data is the average value (n = 6). Different lower-case letters indicate significant differences between tillage treatments ($P < 0.05$).

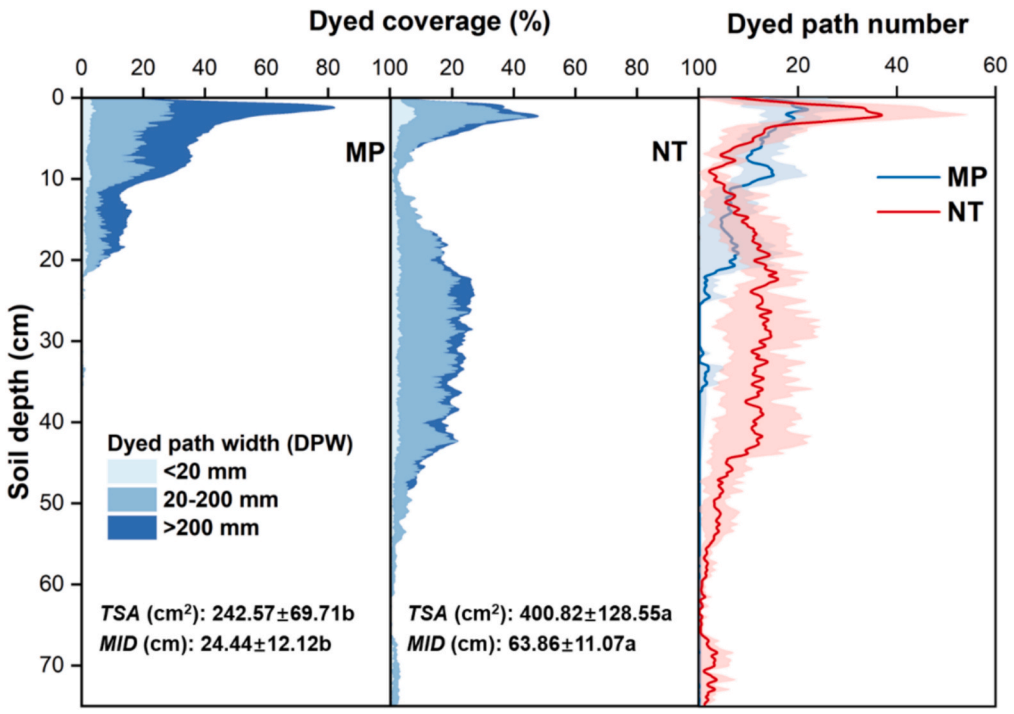


**Fig. 3.** The total stained area (*TSA*), maximum infiltration depth (*MID*), dyed coverage for three dyed path width (*DPW*) (<20, 20–200, and >200 mm), and dyed path number with soil depth under no-tillage (NT) and moldboard plough (MP). The data is the average value (n = 6). The shaded area is the standard deviation. Different lower-case letters indicate significant differences in *TSA* or *MID* between tillage treatments ($P < 0.05$).

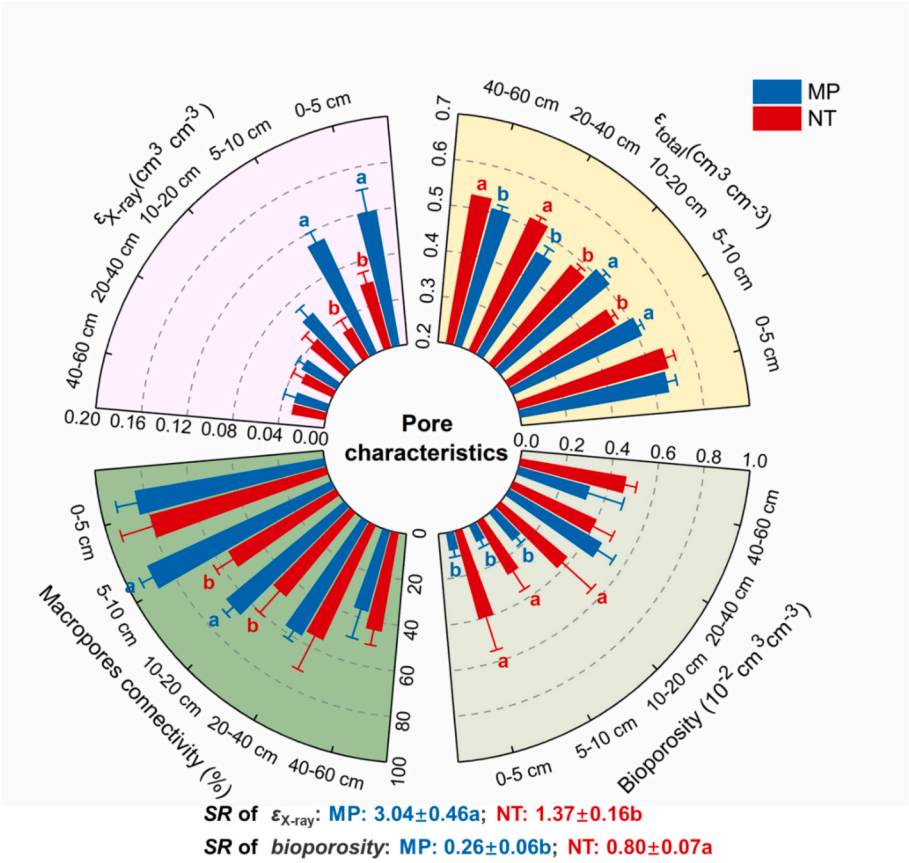


**Fig. 4.** Pore characteristics in the 0–60 cm soil profile under no-tillage (NT) and moldboard plough (MP). $\varepsilon_{total}$ is the total porosity. $\varepsilon_{X\text{-}ray}$ is the macroporosity derived from X-ray CT. *SR* is the stratification ratio of $\varepsilon_{X\text{-}ray}$ and bioporosity (0–20 cm/20–60 cm). The data is the average value (n = 5). Different lower-case letters indicate significant differences between tillage treatments at the same soil depth ($P < 0.05$).

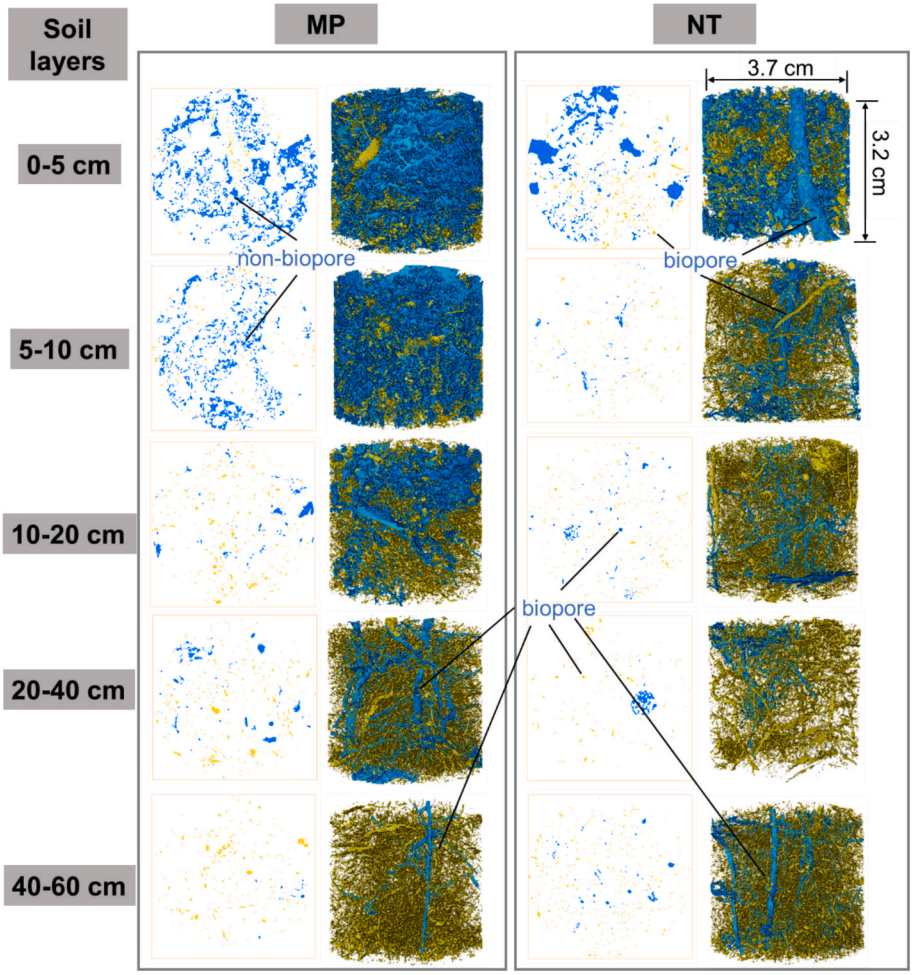


**Fig. 5.** 3D visualizations of soil cores of no-tillage (NT) and moldboard plough (MP) in the 0–5, 5–10, 10–20, 20–40, and 40–60 cm soil layers, respectively. The blue color represents connected pores from top to bottom of the core, and the yellow color represents isolated pores.

*2.6.2. Statistical analysis*

Statistical analyses were performed to compare tillage treatment effects on hydrological and pore characteristics. Student's *t*-test assessed differences in ponding depth, *MID*, $S_t$, $V_{wf}$, $S_{mean}$, *TSA*, and pore parameters after verifying data normality through residual plot inspection. We conducted one-way ANOVA to compare pore characteristics and macropore clogging rates across treatments. All analyses were performed with SPSS Statistics 24.0 (IBM, Armonk, NYC, USA).

We employed structural equation modeling (SEM) using IBM SPSS AMOS 24.0 (IBM, Armonk, NYC, USA) to examine causal relationships among variables. The models were developed through an iterative process of construction, validation, and adjustment. Using maximum likelihood estimation, we derived standardized path coefficients to quantify both the magnitude and direction of variable relationships.

## 3. Results

### *3.1. Characteristics of water infiltration under contrasting tillage practices*

Water infiltration behavior differed markedly between the NT and MP systems. During one hour of simulated rainfall, NT maintained minimal surface ponding (0.12 cm). In contrast, MP developed substantial ponding (0.92 cm) within just 10 min, reaching 2.24 cm after one hour- a value 18 times higher than under NT ($P < 0.05$) (Table 1). Cumulative infiltration depths also varied markedly: while both treatments reached 5 cm after 6 min, NT showed substantially deeper infiltration thereafter, reaching >60 cm after 60 min, comparing to only 40 cm under MP (Fig. 2a). The *MID* under MP (40 cm) was notably lower than under NT (60 cm), and the $S_t$ values further confirmed this trend (6.74 mm for MP vs. 13.67 mm for NT, $P < 0.05$) (Table 1). Additionally, $V_{wf}$ at depths at the 20, 30, and 40 cm depths under MP was significantly lower ($P < 0.05$) than under NT, while $S_{mean}$ was lower at most depths except 10 cm, where MP showed higher saturation ($P < 0.05$) (Fig. 2b, c).

Dye tracer experiments provided further insight into the mechanisms driving these infiltration patterns. The *TSA* and *MID* under NT were 1.7 and 2.6 times greater, respectively, than under MP ($P < 0.05$) (Fig. 3), indicating more extensive water movement in NT soils. Under MP, dyed coverage and the number of stained pathways decreased steadily with depth. In contrast, NT exhibited dynamic flow pathways: dye coverage initially increased (0–5 cm), declined (5–10 cm), and then expanded again at greater depths, suggesting preferential flow through biopores or root channels. Notably, MP had 32.8 % dye coverage in the 0–15 cm layer, more than double that of NT (14.3 %), but this trend reversed in deeper layers (Fig. 3). Dye pathway width also differed: MP predominantly featured wider paths (20–200 and >200 mm), while NT had a higher proportion intermediate-width path (20–200 mm). Pathway counts were higher under NT in the 0–5 cm and deeper layers but lower in the 5–15 cm layer compared to MP. These results highlight that NT promotes more heterogeneous and deeper water penetration, whereas MP restricts flow to narrower, shallower pathways.

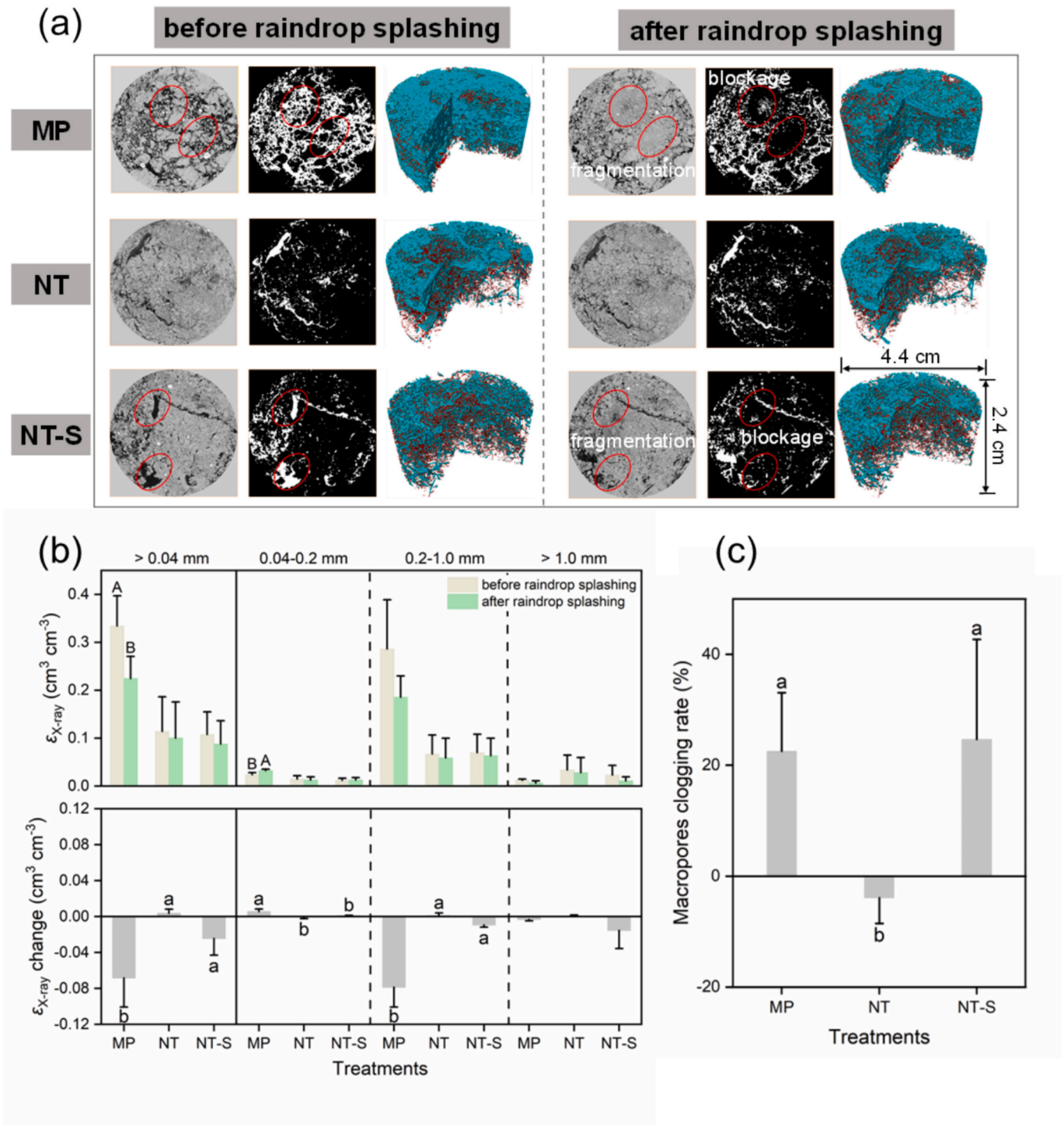


**Fig. 6.** The 3D visualizations of soil cores (a), macroporosity derived from X-ray CT ($\varepsilon_{X\text{-}ray}$), their changes (b), and macropores clogging rate (c) before and after raindrop splashing under moldboard plough (MP), no-tillage (NT), and no-tillage without straw mulch (NT-S) in the top part (0.1–2.4 cm). The gray color represents pores with a pore size of 40–200 μm and the cyan color represents pores with a pore size greater than 200 μm. The data is the average value (n = 6). Different upper-case letters indicate significant differences between before and after raindrop splashing at the same treatment ($P < 0.05$). Different lower-case letters indicate significant differences between treatments ($P < 0.05$).

### *3.2. Characteristics of soil pores and their changes during rainfall under contrasting tillage practices*

The distribution and stability of soil pores varied significantly between NT and MP systems. While the $\varepsilon_{total}$ in the 0–5 cm layer was similar between the two treatments ($P > 0.05$), MP exhibited higher $\varepsilon_{total}$ in the 5–20 cm layer but lower $\varepsilon_{total}$ in deeper layers (20–60 cm) compared to NT ($P < 0.05$) (Fig. 4). X-ray-measured porosity further highlighted these contrasts: MP had 2.0× and 3.6× higher $\varepsilon_{X\text{-}ray}$ than NT in the 0–5 cm and 5–10 cm layers, respectively ($P < 0.05$), but no differences were observed below 10 cm ($P > 0.05$) (Fig. 4). Macropore connectivity in MP was 63.2 % and 60.8 % higher than NT in the 5–10 and 10–20 cm layers ($P < 0.05$), whereas NT maintained greater vertical biopore abundance and higher bioporosity across most depths (Figs. 4

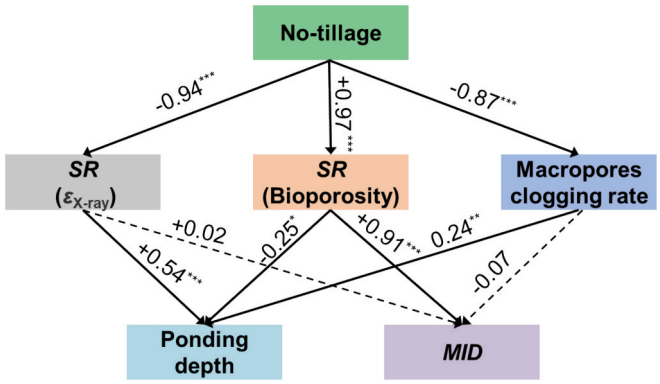


**Fig. 7.** Structural equation model (SEM) depicting how no-tillage affect soil infiltration capacity and how far this is mediated by soil properties. $\varepsilon_{X\text{-ray}}$ is the macroporosity derived from X-ray CT. *SR* is the stratification ratio of $\varepsilon_{X\text{-ray}}$ and bioporosity in the 0–20 and 20–60 cm layers. *MID* is maximum infiltration depth. Numbers next to arrows indicate standardized path coefficients. Solid lines indicate significant relationships, and dash lines indicate non-significant pathways. *, **, *** indicate significant differences at 0.05, 0.01 and 0.001 levels, respectively. The parameters of model are $\chi^2/df = 1.042$, CFI = 0.998, RMSEA = 0.062.

and 5). These structural differences were reflected in the *SR* value: MP had a higher *SR* for $\varepsilon_{X\text{-ray}}$ (3.04 vs. 1.37) but a lower *SR* for bioporosity (0.26 vs. 0.80) compared to NT (Fig. 4), suggesting that NT fosters more stable, biologically mediated pore networks.

Raindrop splashing exerted distinct effects on pore structure, with impacts diminishing with soil depth. Below 2.4 cm, $\varepsilon_{X\text{-ray}}$ remained unchanged across treatments (Fig. S5). Surface macroaggregates under MP were particularly susceptible to raindrop disruption, forming irregular depressions (Fig. 6a and S6). In the 0.1–2.4 cm layer, MP experienced a 20.4 % decline in $\varepsilon_{X\text{-ray}}$ (>0.04 mm) post-rainfall ($P < 0.05$), driven by the collapse of 0.2–1.0 mm pores and a compensatory increase in 0.04–0.2 mm pores ($P < 0.05$) (Fig. 6b). In contrast, NT and NT-S showed no significant changes ($P > 0.05$), and pores >1.0 mm were unaffected in all treatments. Notably, the macropore clogging rate was lower in NT than in MP and NT-S ($P < 0.05$), though MP and NT-S did not differ significantly ($P > 0.05$) (Fig. 6c). These results demonstrate that NT mitigates raindrop-induced pore degradation, preserving infiltration capacity by maintaining larger, more stable pores.

## 4. Discussion

Our results demonstrated that NT significantly enhances soil infiltration capability compared to MP during heavy rainfall, as evidenced by delayed ponding onset, reduced surface water accumulation, and a greater *MID* (Table 1). Results from soil moisture sensors revealed that NT facilitated earlier water arrival in deeper layers (Fig. 2a), aligning with $Br^-$ trace results by Hess et al. (2018) and supporting the hypothesis that NT promotes bypass flow through preferential pathways, whereas MP retains water in upper layers via matrix flow (Kulasekera et al., 2011). Dye tracer experiments further validated this result: MP exhibited higher topsoil *TSA*, indicative of lateral matrix flow, while NT showed deeper, vertically oriented pathways (Fig. 3).

Rainfall infiltration is primarily governed by soil pore architecture and surface conditions (Almeida et al., 2018). In this study, we evaluated pore structure by defining connected macropores as those forming continuous pathways from the top to the bottom of the soil sample (Lu et al., 2019). It is well-established that pore connectivity generally increases with $\varepsilon_{X\text{-ray}}$, particularly when $\varepsilon_{X\text{-ray}}$ is below a threshold of approximately 0.1 $cm^3$ $cm^{-3}$ (Jarvis et al., 2017; Tian et al., 2019). While this relationship explains why the 5–20 cm layer under MP exhibited greater connected macroporosity than under NT, our findings demonstrate that infiltration capacity is controlled by the integrated pore characteristics across the entire soil profile, not just within an individual layer.

Critically, MP management led to a highly stratified pore system with a significantly higher *SR* of porosity (Fig. 4). Structural equation modelling (SEM) revealed that this stratified macropore distribution under MP exacerbated surface ponding and significantly restricted the *MID* ($P < 0.05$) (Fig. 7). We attribute this to plow pan formation, which disrupts vertical pore continuity and promotes lateral water flow (Alletto et al., 2011; Jiang et al., 2017). In contrast, the NT system fostered a more hydrologically efficient and homogeneous pore network, characterized by greater biopore continuity and a lower macroporosity stratification ratio. the NT soil profile significantly reduced ponding and facilitated deep infiltration ($P < 0.05$) (Figs. 4 and 7). This enhanced performance is largely due to the prevalence of stable, vertical biopores formed by decayed roots and earthworm activity, which act as effective conduits for transmitting water and air through the soil profile, thereby enhancing overall permeability (Budhathoki et al., 2022; Wardak et al., 2024; Zhang et al., 2019).

Raindrop kinetic energy displaces soil particles, but its effects are tillage-dependent. MP exhibited 20.4 % greater macropore clogging in the 0.1–2.4 cm layer ($P < 0.05$), driven by aggregate breakdown into 0.04–0.2 mm pores (Fig. 6b), which compact into low-permeability crusts (Ma et al., 2022; Qin et al., 2022). NT's straw mulch mitigated this by dissipating raindrop energy, reducing splash erosion and pore clogging (Almeida et al., 2018; Wang et al., 2020). Thus, NT's dual advantages, i.e., stable surface protection and vertically connected pores, collectively enhance infiltration resilience during heavy rainfall.

In regions like Northeast China, where extreme rainfall events are increasing (Fig. S2), NT systems reduce waterlogging risks by accelerating infiltration and minimizing surface runoff. The mulch layer in NT further prevents erosion and preserves soil structure, making it a dual-purpose solution for heavy rainfall and drought (Liu et al., 2020). However, adoption requires addressing practical barriers: (1) initial yield variability during NT transition (Blanco-Canqui et al., 2017) and (2) site-specific adaptation, as NT's benefits are more pronounced in well-structured soils than in compacted or clay-rich fields (Soracco et al., 2019).

## 5. Conclusion

Our findings confirm that long-term no-tillage (NT) enhances infiltration capacity during extreme rainfall events through two synergistic mechanisms: (1) preservation of vertically continuous biopores that maintain profile-wide preferential flow pathways, and (2) surface protection by straw mulch that prevents pore sealing from raindrop impact. In contrast, moldboard plow (MP) systems exhibit compromised infiltration due to structural disruption of pore networks and lack of protective surface cover. These results directly support our hypothesis that NT systems are functionally superior to MP in maintaining infiltration capacity under intense precipitation.

Our findings underscore NT as a holistic soil management strategy that concurrently optimizes pore network functionality and strengthens climate resilience. By integrating structural stability with hydrological efficiency, NT systems offer a sustainable solution for rainfall-dependent agroecosystems facing increasingly erratic precipitation regimes. Future research should quantify the long-term trade-offs between tillage-induced pore evolution and crop productivity across diverse pedoclimatic contexts.

## CRediT authorship contribution statement

**Shijie Qin:** Writing – original draft, Methodology, Investigation, Formal analysis, Data curation. **Zhuo Liu:** Writing – original draft, Formal analysis, Data curation. **Meng Tian:** Writing – review & editing, Funding acquisition. **Lin Liu:** Writing – review & editing. **Wei Hu:** Writing – review & editing. **Richard Whalley:** Writing – review &

editing. **Tusheng Ren:** Writing – review & editing. **Weida Gao:** Writing – review & editing, Writing – original draft, Funding acquisition.

## Declaration of competing interest

The authors declare that they have no known competing financial interests or personal relationships that could have appeared to influence the work reported in this paper.

## Acknowledgements

This work is supported by National Key Research and Development Program of China (2023YFD1500301), and the National Natural Science Foundation of China (No. 42407436).

## Appendix A. Supplementary data

Supplementary data to this article can be found online at https://doi.org/10.1016/j.geoderma.2025.117542.

## Data availability

Data will be made available on request.

## References

Allaire-Leung, S.E., Gupta, S.C., Moncrief, J.F., 2000. Water and solute movement in soil as influenced by macropore characteristics: 1. Macropore continuity. J. Contam. Hydrol. 41 (3–4), 283–301. https://doi.org/10.1016/S0169-7722(99)00079-0.

Alletto, L., Coquet, Y., Vachier, P., Labat, C., 2011. Vertical and lateral variations of soil immobile water fraction in two tillage systems. Soil Sci. Soc. Am. J. 75 (2), 498–508. https://doi.org/10.2136/sssaj2010.0267.

Almeida, W.S., Panachuki, E., Oliveira, P.T.S., Silva Menezes, R., Sobrinho, T.A., Carvalho, D.F., 2018. Effect of soil tillage and vegetal cover on soil water infiltration. Soil Tillage Res. 175, 130–138. https://doi.org/10.1016/j.still.2017.07.009.

Assouline, S., 2004. Rainfall-induced soil surface sealing: a critical review of observations, conceptual models, and solutions. Vadose Zone J. 3 (2), 570–591. https://doi.org/10.2136/vzj2004.0570.

Blanco-Canqui, H., Wienhold, B.J., Jin, V.L., Schmer, M.R., Kibet, L.C., 2017. Long-term tillage impact on soil hydraulic properties. Soil Tillage Res. 170, 38–42. https://doi.org/10.1016/j.still.2017.03.001.

Budhathoki, S., Lamba, J., Srivastava, P., Williams, C., Arriaga, F., Karthikeyan, K.G., 2022. Impact of land use and tillage practice on soil macropore characteristics inferred from X-ray computed tomography. Catena 210, 105886. https://doi.org/10.1016/j.catena.2021.105886.

Cynthia, R., Tubiello, F.N., Goldberg, R., Mills, E., Bloomfield, J., 2002. Increased crop damage in the US from excess precipitation under climate change. Glob. Environ. Chang. 12, 197–202. https://doi.org/10.1016/S0959-3780(02)00008-0.

Fan, R., Zhang, X., Yang, X., Liang, A., Jia, S., Chen, X., 2013. Effects of tillage management on infiltration and preferential flow in a black soil, Northeast China. Chin. Geogr. Sci. 23, 312–320. https://doi.org/10.1007/s11769-013-0606-9.

Fernández-Ugalde, O., Virto, I., Bescansa, P., Imaz, M.J., Enrique, A., Karlen, D.L., 2009. No-tillage improvement of soil physical quality in calcareous, degradation-prone, semiarid soils. Soil Tillage Res. 106, 29–35. https://doi.org/10.1016/j.still.2009.09.012.

Fischer, E.M., Knutti, R., 2015. Anthropogenic contribution to global occurrence of heavy-precipitation and high-temperature extremes. Nat. Clim. Chang. 5, 560–564. https://doi.org/10.1038/nclimate2617.

German-Heins, J., Flury, M., 2000. Sorption of Brilliant Blue FCF in soils as affected by pH and ionic strength. Geoderma 97, 87–101. https://doi.org/10.1016/S0016-7061(00)00027-6.

Gómez-Paccard, C., Hontoria, C., Mariscal-Sancho, I., Pérez, J., León, P., González, P., Espejo, R., 2015. Soil-water relationships in the upper soil layer in a Mediterranean Palexerult as affected by no-tillage under excess water conditions-Influence on crop yield. Soil Tillage Res. 146, 303–312. https://doi.org/10.1016/j.still.2014.09.012.

Govindasamy, P., Mowrer, J., Rajan, N., Provin, T., Hons, F., Bagavathiannan, M., 2020. Influence of long-term (36 years) tillage practices on soil physical properties in a grain sorghum experiment in Southeast Texas. Arch. Gron. Soil Sci. 67, 234–244. https://doi.org/10.1080/03650340.2020.1720914.

Guo, Z., 2020. Estimating method of maximum infiltration depth and soil water supply. Sci. Rep. 10. https://doi.org/10.1038/s41598-020-66859-0.

Haruna, S.I., Mosley, C., Downs, K.M., O'Brien, K., Carter, J.G., 2024. Effects of cover crop and tillage management practices on in situ and ex situ water infiltration parameters. Arch. Gron. Soil Sci. 70 (1), 1–17. https://doi.org/10.1080/03650340.2024.2434086.

Hess, L.J.T., Hinckley, E.-L.-S., Robertson, G.P., Hamilton, S.K., Matson, P.A., 2018. Rainfall intensification enhances deep percolation and soil water content in tilled and no-till cropping systems of the US Midwest. Vadose Zone J. 17, 1–12. https://doi.org/10.2136/vzj2018.07.0128.

Hildebrand, T., Rüegsegger, P., 1997. A new method for the mode-independent assessment of thickness in three-dimensional images. J. Microsc. 185, 67–75. https://doi.org/10.1046/j.1365-2818.1997.1340694.x.

Houston, A.N., Otten, W., Falconer, R., Monga, O., Baveye, P.C., Hapca, S.M., 2017. Quantification of the pore size distribution of soils: assessment of existing software using tomographic and synthetic 3D images. Geoderma 299, 73–82. https://doi.org/10.1016/j.geoderma.2017.03.025.

Hu, H., Wen, J., Peng, Z., Tian, F., Tie, Q., Lu, Y., Khan, M.Y.A., 2019. High-frequency monitoring of the occurrence of preferential flow on hillslopes and its relationship with rainfall features, soil moisture and landscape. Hydrol. Sci. J. 64, 1385–1396. https://doi.org/10.1080/02626667.2019.1638513.

Jarvis, N., Larsbo, M., Koestel, J., 2017. Connectivity and percolation of structural pore networks in a cultivated silt loam soil quantified by X-ray tomography. Geoderma 639 (287), 71–79. https://doi.org/10.1016/j.geoderma.2016.06.026.

Jiang, X.J., Liu, S., Zhang, H., 2017. Effects of different management practices on vertical soil water flow patterns in the Loess Plateau. Soil Tillage Res. 166, 33–42. https://doi.org/10.1016/j.still.2016.10.001.

Kulasekera, P.B., Parkin, G.W., Bertoldi, P.V., 2011. Using soil water content sensors to characterize tillage effects on preferential flow. Vadose Zone J. 10 (2), 683–696. https://doi.org/10.2136/vzj2010.0063.

Legout, C., Legúedois, S., Le Bissonnais, Y., Malam Issa, O., 2005. Splash distance and size distributions for various soils. Geoderma 124 (3–4), 279–292. https://doi.org/10.1016/j.geoderma.2004.05.006.

Liu, S.Z., Gao, W.D., Ren, T.S., 2020. Evaluating the stability of black soil water content in Northeast China under no tillage and ridge tillage using least limiting water range. Trans. CSAE 36 (10), 107–115. https://doi.org/10.11975/j.issn.1002-6819.2020.10.013.

Lu, S., Yu, X., Zong, Y., 2019. Nano-microscale porosity and pore size distribution in aggregates of paddy soil as affected by long-term mineral and organic fertilization under rice-wheat cropping system. Soil Tillage Res. 186, 191–199. https://doi.org/10.1016/j.still.2018.10.008.

Lucas, M., Schlüter, S., Vogel, H.J., Vetterlein, D., 2019. Soil structure formation along an agricultural chronosequence. Geoderma 350, 61–72. https://doi.org/10.1016/j.geoderma.2019.04.041.

Ma, G., Li, G., Mu, X., Hou, W., Ren, Y., Yang, M., 2022. Effect of raindrop splashes on topsoil structure and infiltration characteristics. Catena 212, 106040. https://doi.org/10.1016/j.catena.2022.106040.

Marquart, A., Goldbach, L., Blaum, N., 2020. Soil-texture affects the influence of termite macropores on soil water infiltration in a semi-arid savanna. Ecohydrology 13, e2249.

Mestelan, S., Smeck, N., Sprunger, C., Dyck, A., Dick, W., 2021. Four decades of continuously applied tillage or no-tillage on soil properties and soil morphology. Agrosyst. Geosci. Environ. 4 (3), e20195. https://doi.org/10.1002/agg2.20195.

Moraes, M.T., Debiasi, H., Carlesso, R., Franchini, J.C., Silva, V.R., Luz, F.B., 2016. Soil physical quality on tillage and cropping systems after two decades in the subtropical region of Brazil. Soil Tillage Res. 155, 351–362. https://doi.org/10.1016/j.still.2015.07.015.

Pagenkemper, S.K., Athmann, M., Uteau, D., Kautz, T., Peth, S., Horn, R., 2015. The effect of earthworm activity on soil bioporosity-Investigated with X-ray computed tomography and endoscopy. Soil Tillage Res. 146, 79–88. https://doi.org/10.1016/j.still.2014.05.007.

Piao, S., Ciais, P., Huang, Y., Shen, Z., Peng, S., Li, J., Zhou, L., Liu, H., Ma, Y., Ding, Y., Friedlingstein, P., Liu, C., Tan, K., Yu, Y., Zhang, T., Fang, J., 2010. The impacts of climate change on water resources and agriculture in China. Nat 467, 43–51. https://doi.org/10.1038/nature09364.

Qin, S., Shi, D., Gao, W., 2022. Responses of soil water content to rainfall events under different tillage management in Southern Jilin Province of China. Trans. CSAE 38, 147–155. https://doi.org/10.11975/j.issn.1002-6819.2022.18.016.

Soil Survey Staff, 2022. Keys to Soil Taxonomy, 13th ed. USDA-Natural Resources Conservation Service. https://www.nrcs.usda.gov/sites/default/files/2022-09/Keys-to-Soil-Taxonomy.pdf.

Soracco, C.G., Villarreal, R., Melani, E.M., Oderiz, J.A., Salazar, M.P., Otero, M.F., Irizar, A.B., Lozano, L.A., 2019. Hydraulic conductivity and pore connectivity. Effects of conventional and no-till systems determined using a simple laboratory device. Geoderma 337, 1236–1244. https://doi.org/10.1016/j.geoderma.2018.10.045.

Tian, J., Zhang, B., He, C., Han, Z., Bogena, H.R., Huisman, J.A., 2019. Dynamic response patterns of profile soil moisture wetting events under different land covers in the Mountainous area of the Heihe River Watershed, Northwest China. Agric. For. Meteorol. 271, 225–239. https://doi.org/10.1016/j.agrformet.2019.03.006.

Wang, L., Zhang, G., Zhu, P., Wang, X., 2020. Comparison of the effects of litter covering and incorporation on infiltration and soil erosion under simulated rainfall. Hydrol. Process. 34, 2911–2922. https://doi.org/10.1002/hyp.13779.

Wardak, D.L.R., Padia, F.N., Heer, M.I., Sturrock, C.J., Mooney, S.J., 2024. Zero-tillage induces significant changes to the soil pore network and hydraulic function after 7 years. Geoderma 447, 116934. https://doi.org/10.1016/j.geoderma.2024.116934.

Weiler, M., Flühler, H., 2004. Inferring flow types from dye patterns in macroporous soils. Geoderma 120, 137–153. https://doi.org/10.1016/j.geoderma.2003.08.014.

Yudina, A.V., Klyueva, V.V., Romanenko, K.A., Fomin, D.S., 2022. Micro-within macro: how micro-aggregation shapes the soil pore space and water-stability. Geoderma 415, 115771. https://doi.org/10.1016/j.geoderma.2022.115771.

Zhang, Z., Liu, K., Zhou, H., Lin, H., Li, D., Peng, X., 2019. Linking saturated hydraulic conductivity and air permeability to the characteristics of biopores derived from X-ray computed tomography. J. Hydrol. 571, 1–10. https://doi.org/10.1016/j.jhydrol.2019.01.041.

Zwartendijk, B.W., van Meerveld, H.J., Ghimire, C.P., Bruijnzeel, L.A., Ravelona, M., Jones, J.P.G., 2017. Rebuilding soil hydrological functioning after Swidden agriculture in eastern Madagascar. Agric. Ecosyst. Environ. 239, 101–111. https://doi.org/10.1016/j.agee.2017.01.002.